Journal of Alloys and Compounds 695 (2017) 3094–3103

Contents lists available at ScienceDirect

Journal of Alloys and Compounds

journal homepage: http://www.elsevier.com/locate/jalcom

Photoluminescent properties of ZrO_2: Tm^{3+}, Tb^{3+}, Eu^{3+} powders—A combined experimental and theoretical study

L.X. Lovisa [a, *], J. Andrés [b], L. Gracia [b], M.S. Li [c], C.A. Paskocimas [a], M.R.D. Bomio [a], V.D. Araujo [d], E. Longo [e], F.V. Motta [a]

[a] DEMAT, CT, UFRN, Av. Sen. Salgado Filho, 3000, CEP 59072-970 Natal, RN, Brazil
[b] Departament de Química Física i Analítica, Universitat Jaume I, Campus del Riu Sec, Castelló E-12071, Spain
[c] IFSC, USP, Av. Trabalhador São Carlense, 400, CEP 13566-590 São Carlos, SP, Brazil
[d] UFRPE, Av. Rua Dom Manoel de Medeiros, CEP52171-900 Recife, PE, Brazil
[e] LIEC, IQ, UNESP, Rua Francisco Degni s/n, CEP 14801-907 Araraquara, SP, Brazil

ARTICLE INFO

Article history:
Received 12 May 2016
Received in revised form
14 November 2016
Accepted 23 November 2016
Available online 25 November 2016

Keywords:
ZrO_2:RE
Photoluminescence
DFT calculations
White LEDs

ABSTRACT

Rare-earth (RE) element-based materials for optical applications have received increasing attention owing to the emission properties of RE ions, which render these materials suitable for use in color displays, lasers, and solid-state lighting. In the present work, ZrO_2:RE (RE = Tm^{3+}, Tb^{3+}, and Eu^{3+}) powders were obtained via complex polymerization, and characterized by means of X-ray diffraction (XRD), Raman spectroscopy, UV–visible absorption spectroscopy, and photoluminescence measurements. The XRD patterns and Raman spectra revealed the tetragonal phase of ZrO_2 co-doped with up to 4 mol.% RE^{3+} and stabilization of the cubic phase, for up to 8 mol.% RE^{3+}. In addition, the photoluminescence measurements revealed simultaneous emissions in the blue (477 nm), green (496.02 nm and 548.32 nm), and red-orange (597.16 nm and 617.54 nm) regions. These emissions result from the Tm^{3+}, Tb^{3+}, and Eu^{3+} ions, respectively. Energy transfers, such as $^1G_4$ levels (Tm^{3+}) → $^5D_4$ (Tb^{3+}) and $^5D_4$ levels (Tb^{3+}) → $^5D_0$ (Eu^{3+}), occurred during the emission process. Calculations based on density functional theory (DFT) were performed, to complement the experimental data. The results revealed that structural order/disorder effects were generated in the cubic and tetragonal ZrO_2 phases in the ZrO_2:Eu^{3+} powders, and changes in the electronic structure were manifested as a decrease in the band gap values. The chromaticity coordinates of all the samples were determined from the PL spectrum. The coordinates, x = 0.34 and y = 0.34, of the ZrO_2:8%RE sample corresponded to a point located in the white region of the CIE diagram and color correlated temperature (CCT) was found to be 5181 K. More importantly, the present results indicate that ZrO_2:RE powders constitute promising photoluminescent materials for use in new lighting devices.

1. Introduction

The synthesis and characterization of rare earth (RE)-doped nanomaterials have been extensively investigated. These materials have excellent properties [1,2], such as narrow emission bandwidths (<10 nm), long luminescence lifetime, high photostability, and low toxicity [3,4]. In recent years, these materials have received considerable attention owing to their use in several important applications, such as multiplexed imaging and sensing, bioassays, and multiplex biodetection [5–14]. The development of luminescent materials, which are more efficient than those currently available, is extremely challenging. Moreover, the use of a suitable host material for the RE ions is essential for achieving high efficiency [15].

Zirconium dioxide or zirconia (ZrO_2) and ZrO_2-based materials constitute an appropriate host for RE, owing to a unique combination of different properties. These include: high refractive index, large optical band gap, low optical loss, and high transparency in the visible and near-infrared regions, good chemical stability [16,17], and lower phonon frequency (~470 cm^{-1}) than other matrices such as Y_2O_3 (~597 cm^{-1}) and TiO_2 (~700 cm^{-1}) [18]. As such, the luminescence efficiency of active ions may be improved

* Corresponding author.
E-mail address: lovisaengmat@ig.com.br (L.X. Lovisa).

http://dx.doi.org/10.1016/j.jallcom.2016.11.341
0925-8388/

via incorporation into the ZrO_2 matrix [19].

RE ions can enhance the emission of photoluminescent materials, and the corresponding energy transfer (ET) process occurs between an ion donor (D) and an ion acceptor (A). During the ET process, the energy of D (which is in an excited electronic state) is transferred to A. Specific conditions must be fulfilled in order to realize this mechanism. These include: (i) the emission band of D is partially superimposed on the absorption band of A, and (ii) the distance (R) between D and A must be sufficiently short, since the energy transfer efficiency is proportional to $1/R^6$, to enable interaction of the dipole–dipole emission bands of the material [20]. These unique properties have led to the widespread use of RE ions in optical devices.

Direct excitation of Eu^{3+} ions is a relatively inefficient process, owing to the forbidden nature of the 4f transitions. However, Eu-doped inorganic materials may exhibit efficient luminescence emissions upon ultraviolet excitation. These materials also exhibit a large Stokes shift, sharp emission spectrum, and have a long lifetime, high chemical/photochemical stability, low toxicity, and reduced photobleaching, owing to shielding of the 4f electrons [21]. As such, Quan et al. [22] obtained spherical ZrO_2:Eu^{3+} particles by using a spray drying process followed by a post annealing treatment. Gedanken et al. [23] used a sonochemical method for the europium-oxide doping of ZrO_2 nanoparticles. Furthermore, Tiwari et al. [24] determined the effect of varying Eu^{3+} concentration on the photo- and thermoluminescence of ZrO_2 nanophosphors. Some RE ion-doped ZrO_2 materials, such as ZrO_2:Eu [25], ZrO_2:Tb [26], and ZrO_2:Tm [27], have interesting properties. Vidya et al. [28] investigated the color-tunable photoluminescence photocatalytic activities and phase transformation of a ZrO_2:Tb^{3+} nanophosphor. Mari et al. [29] determined the photoluminescence properties of Tb^{3+} in ZrO_2 zirconia host matrices (prepared via combustion synthesis) at different calcination temperatures.

Shang et al. [30] examined the process of energy transfer between Tm^{3+} and Ho^{3+} excited by a UV nanocrystal-LaOF laser and classified the interaction between the ions as a quadrupole-quadrupole type of interaction. Joshi [31] examined the energy transfer from Tb^{3+} and Eu^{3+} in zinc phosphate glasses and concluded that these ions undergo mainly dipole-dipole interactions. Moreover, the efficiency of this transfer was highest at a concentration of 8.6 mol% Eu^{3+}. The emissions of Tm^{3+}, Eu^{3+}, and Tb^{3+} ions fall within the blue, red, and green regions, respectively, of the visible spectrum [32–34]. Particles that have tunable emission colors are obtained from a combination of lanthanide ions in a host material. The first-ever generation of white light from the simultaneous emission of blue, green, and red, under UV excitation, was obtained for borate-based glasses co-doped with Ce^{3+}, Tb^{3+}, and Mn^{3+} [35]. Furthermore, the spectra of Tm^{3+}, Tb^{3+}, and Sm^{3+} co-doped silicate glass, which was excited in the near-UV region, exhibited bands corresponding to blue, green, and orange-red emissions [36].

This paper can be considered a prolongation of previously work (CITA) in which the main focus is the investigation of the photoluminescent properties of the particles of ZrO_2 co-doped with Tm^{3+}, Tb^{3+}, and Eu^{3+}, by using the polymerization method [37–40]. The use of the complex polymerization method in the research materials is widespread because it presents advantages such as good homogeneous distribution of different metal ions along the polymer formed, facilitating control stoichiometric. Other positive aspects of the method are the low temperature synthesis, obtaining nanometric particles and reproducibility. At this time, we will examine the effect of the concentration of RE (mol%) in the discussed property. In addition, first-principle calculations were performed in order to explain the structural and electronic changes induced by the doping of ZrO_2:Eu. The energy transfer processes between Tm^{3+} and Tb^{3+} and between Tb^{3+} and Eu^{3+}, were also discussed. X-ray diffraction (XRD), Raman spectroscopy, UV–visible reflectance spectroscopy, and photoluminescence (PL) measurements were used to characterize the samples. Moreover, a chromaticity diagram was determined from emission spectra data, in order to verify the efficiency of these materials during the emission of white light.

The remainder of this paper is organized as follows: Section 2 describes the synthesis method, characterization techniques, and computational details; Sections 3 and 4 present the results and conclusions, respectively.

2. Experimental section

2.1. Synthesis of ZrO_2:RE powders

The samples were prepared by using a complex polymerization method. During the synthesis, the zirconium citrate was obtained by dissolving zirconium nitrate (Vetec, 99%) in an aqueous citric acid solution, under agitation, at a temperature of ~80 °C. Doping was performed by adding cations of RE to the solution. A europium solution and a thulium solution were prepared by dissolving Eu_2O_3 (Aldrich, 99.9%) and Tm_2O_3 (Aldrich, 99.9%), respectively, in nitric acid. Each solution was then separately mixed with the zirconium citrate solution. Terbium nitrate (Aldrich, 99.9%) was subsequently added to the mixed solution. Furthermore, ethylene glycol was added to the solution, under constant stirring, in order to promote polymerization of the citrate, through the polyesterification reaction. The molar ratio between citric acid and ethylene glycol used was set to 60/40 (mass ratio). After 4 h, water was completely removed, thereby yielding a translucent resin. Various (1, 2, 4 and 8 mol % of RE) dopant concentrations were considered. This percentage of RE is on the contribution of all dopants, such as: ZrO_2: 1% RE, ZrO_2: 2%RE, ZrO_2: 4%RE and ZrO_2: 8%RE correspond respectively to $Zr_{0.99}O_2$: $_{0.0033}$ $Tb_{0.0033}$ $Tm_{0.0034}$ Eu, $Zr_{0.98}O_2$: $_{0.0066}$ $Tb_{0.0066}$ $Tm_{0.0068}$ Eu, $Zr_{0.96}O_2$: $_{0.0133}$ $Tb_{0.0133}$ $Tm_{0.0134}$ Eu and $Zr_{0.92}O_2$: $_{0.0266}$ $Tb_{0.0266}$ $Tm_{0.0268}$ Eu. The polymeric resin was heat-treated at 350 °C (10 °C/min) for 4 h, leading to partial decomposition of the polymeric gel; this resulted in the formation of an expanded resin, which consisted of partially pyrolyzed material. The resulting powders were annealed at 600 °C for 2 h at a heating rate of 10 °C/min.

2.2. Characterization of ZrO_2:RE (RE = Tm^{3+}, Tb^{3+}, and Eu^{3+}) powders

The as-synthetized powders were examined by XRD (Shimadzu diffractometer model XRD–7000), using Cu-Kα radiation. In addition, Raman spectrometry (Horiba Jobin-Yvon Raman Labram) was performed at room temperature; an Olympus BX41 TM microscope equipped with a 514 nm-wavelength laser, was used as the excitation source. UV–vis reflectance spectra (Cary model 5G) and PL spectra (Thermal Jarrel-AshMonospec 27 monochromator and Hamatsu R446 photomultiplier) of the ZrO_2:RE particles were also obtained. A 350.7 nm-wavelength laser with krypton ions (CoherentInnova) and an output of ~13.3 mW, was used as the excitation source during the PL measurements; these measurements were all performed at room temperature. To characterize white light resulting from the aforementioned mixing, we calculated the chromaticity coordinates using the spectrum represented in Fig. 3. The chromaticity coordinates of red (the *x* coordinate), green (the *y* coordinate) and blue (the *z* coordinate) were determined according to the system of the International Commission on Illumination given in 1968 [41,42] using the following relationships:

$$x = \frac{(X)}{(X+Y+Z)} \quad y = \frac{(Y)}{(X+Y+Z)} \quad z = \frac{(Z)}{(X+Y+Z)} \tag{1}$$

where parameters X, Y and Z are the following spectral integrals:

$$X = \int \boldsymbol{x}P(\lambda)d\lambda \quad Y = \int \boldsymbol{y}P(\lambda)d\lambda \quad Z = \int \boldsymbol{z}P(\lambda)d\lambda \tag{2}$$

Here P(λ) is luminescence spectrum of the samples, that provide, for each within the visible range, the emitted intensity. The function P(λ) is determined empirically, the values of λ for components *x*, *y* and *z* are 599, 555 and 446 nm, respectively and ***x***, ***y*** and ***z*** are functions of spectral summarizing. Integrals (2) were calculated through the spectral interval of 350–800 nm. The CCT value was estimated by using McCamy empirical formula [43]. The quality of white light is calculated using McCamy empirical formula in terms of CCT values, which is expressed as:

$$CCT = -449n^3 + 3525n^2 - 6823n + 5520.33 \tag{3}$$

where $n = \frac{(x-xe)}{(y-ye)}$ is the inverse slope line, $xe = 0.332$ and $ye = 0.186$.

2.3. Computational details

First-principle calculations, based on the density functional theory (DFT), were performed by using the Vienna *ab initio* simulation package (VASP). The Kohn-Sham equations were solved by using the Perdew, Burke, and Ernzerhof (PBE) exchange-correlation functional [44], and the electron-ion interaction was described via the projector-augmented-wave pseudo potentials. Moreover, the plane-wave expansion was truncated at a cut-off energy of 520 eV, and the Brillouin zones were sampled by using Monkhorst-Pack special k-point grids. Cubic and tetragonal phases of ZrO_2, both undoped and doped at 12% of Eu substituted for Zr, were considered. In addition, a 12% of Tb and Tm substitutions were tested. The valence electron density is defined by 12 ($4s^2 4p^6 5s^2 4d^2$) electrons for Zr atoms, 6 ($2s^2 2p^4$) electrons for O atoms and 17 ($5s^2 5p^6 6s^2 4f^7$) electrons for Eu atoms. For Tb and Tm atoms, three f-like electrons are treated as core states and 9 electrons are used as valence states for both.

A supercell with 48 atoms was used for both systems, 2 × 2 × 1 and 2 × 2 × 2 for cubic and tetragonal phases, respectively. In the case of 12% doping, two Zr^{4+} were substituted by two Eu^{3+} and oxygen vacancy (both near and far from Eu atoms) was included, to maintain the electroneutrality of the cell. In order to obtain a small amount of Eu doping, extremely large supercells must be used, thereby resulting in a high computational cost. The cell parameters and positions of all atoms were allowed to relax, and the conjugated gradient energy minimization method was used to obtain relaxed systems. This was achieved by setting a threshold value (i.e., 0.01 eV·Å^{-1}) for the forces experienced by each atom. To ensure geometrical and energetic convergence of the cubic and tetragonal ZrO_2 structures, a 3 × 3 × 1 Monkhorst-Pack special k-point grid was used.

3. Results and discussion

3.1. XRD characterization

XRD patterns of pure ZrO_2 and co-doped ZrO_2:xRE (x = 1, 2, and 4%) powders are shown in Fig. 1(a)–(d). Diffraction peaks are located at approximate angles of: 30.07°, 35.02°, 50.28°, 59.87°, 62.60°, and 73.66° corresponding to the (101), (110), (112), (201), (103), and (202) planes, respectively, of the ZrO_2 tetragonal phase

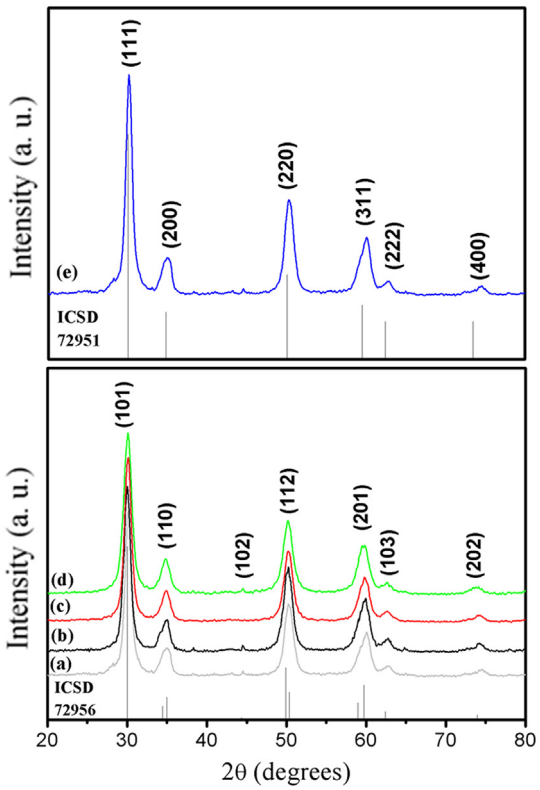

Fig. 1. XRD patterns of (a) non-doped ZrO_2 and ZrO_2:xRE (b) x = 1%, (c) x = 2%, (d) x = 4%, and (e) x = 8%, calcined at 600 °C.

[ICSD 81-1546]. Fig. 1(e) shows the pattern corresponding to ZrO_2:8%RE. In this case, peaks occur at ~29.79°, 34.57°, 50.02°, 59.56°, 62.27°, and 73.35°, corresponding to the (111), (200), (220), (311), (222), and (400) planes, respectively, of the cubic phase of ZrO_2 [ICSD 81-1551]. This phase is stabilized with increasing amount of bi- or trivalent cations introduced into the ZrO_2 structure [45,46]. In addition, the replacement of Zr^{4+} cations by RE^{3+} results in the formation of oxygen vacancies. This leads, in turn, to a change in the lattice parameters of the unit cell (c/a → 1) and consequently, arrangement of the ions in a cubic structure [46]. The ionic radius of oxygen is large, it becomes difficult to maintain the four O^{2-} ions around an ion Zr^{4+} with a fluorite structure (cubic), due to large repulsion between the ions O^{2-}. With the introduction of dopant RE^{3+} replacing Zr^{4+}, there is the appearance of oxygen vacancies in order to offset the charges and as result the force of repulsion between the O^{2-} decreases, giving conditions to accommodate the ions in the cubic structure.

The size of the crystallites in the sample was estimated from the Scherrer equation [47,48] and the full-width half-maximum (FWHM) of an observed peak. The average crystallite size (D) of ZrO_2:RE powders was determined from the strongest peaks corresponding to the (101) tetragonal phase and (111) cubic phase. The lattice parameter (a, c), unit-cell volume (V), and crystallite size of the ZrO_2:RE samples are listed in Table 1.

3.2. Raman characterization

ZrO_2 polymorphism may lead to inaccurate results when the crystalline phases of ZrO_2 are identified only via XRD. Das et al. [45] attributed inaccuracies in XRD identification of tetragonal and cubic phases, to the low angular resolution (0.03°) of the equipment used; this resolution resulted in an overlap of the peaks

Table 1
Value of structural parameters of ZrO_2:xRE (0–8 mol%) nanophosphors.

Parameters	ZrO_2	ZrO_2:1%RE	ZrO_2:2%RE	ZrO_2:4%RE	ZrO_2:8%RE
Crystal System	Tetragonal	Tetragonal	Tetragonal	Tetragonal	Cubic
Space group	$P4_2/nmc$	$P4_2/nmc$	$P4_2/nmc$	$P4_2/nmc$	Fm-3m
2θ	30.0266	29.9272	29.8368	30.1498	29.8368
FWHM (rad)	0.3149	0.7872	0.3149	0.9446	0.3936
Lattice parameters (Å)					
a	3.59756	3.61069	3.60521	3.62814	5.15833
c	5.19462	5.20999	5.19164	5.14336	–
Unit cell volume/formula unit (Å^3)	67.2312	67.9231	67.4786	67.7040	137.2545
Crystallite size (nm)	14.06	14.49	14.79	14.62	12.78

corresponding to these phases. Compared to XRD, Raman spectroscopy can more accurately distinguish among the crystalline phases of ZrO_2 [49]. The band positions, intensities, and shapes can be determined from the Raman spectra. In fact, as shown in Fig. 2 and Table 2, each structure exhibits certain characteristics that correspond to specific locations in the spectra.

The bands that occur at 142, 257, 314, 461, 609, and 627 cm^{-1} in the spectra shown in Fig. 2(a), (b), and (c) are attributed to the vibration modes of tetragonal ZrO_2 [49–51]. The spectrum (d) of the cubic phase of ZrO_2 (fluorite) is characterized by a broad band that occurs at ~605 cm^{-1} [49]. The active modes in the Raman spectra (corresponding to each crystal) and the c/a ratio of the lattice parameters of tetragonal zirconia, are shown in Table 2. Theoretical calculations of the Raman-active modes of pure tetragonal ZrO_2 yield values of 149.4, 294.2, 301.5, 453.6, 611.5, and 650.9 cm^{-1} for the E_g, A_{1g}, B_{1g}, E_g, B_{1g}, and E_g modes, respectively. In the case of pure cubic ZrO_2, a unique mode, which has T_{2g} symmetry, occurs at a wavenumber of 600.7 cm^{-1}. These values concur with previously obtained experimental data.

3.3. UV–visible spectroscopy analysis

The band gap energies of the ZrO_2:RE nanoparticles were estimated from the respective diffuse-reflectance spectra, by plotting the square of the Kubelka–Munk function (i.e., $F(R)^2$) as a function of the energy (in eV). The values were determined by extrapolating the linear part of the curve to $F(R)^2 = 0$, as shown in Fig. 3. The ratio between the molar absorption coefficient (k) and scattering coefficient (s) is estimated from reflectance data using the Kubelka–Munk relation [52] in equation (4):

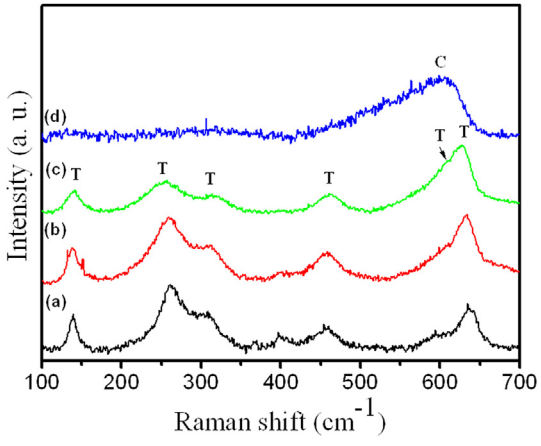

Fig. 2. Raman spectrum of ZrO_2:xRE, (a) x = 1%, (b) x = 2%, (c) x = 4%, and (d) x = 8%.

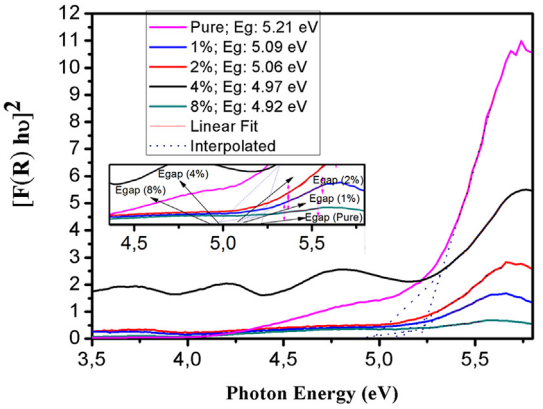

Fig. 3. UV–visible absorption spectra for particles: undoped ZrO_2 and ZrO_2:x% RE (x = 1, 2, 4, and 8% mol).

Table 2
Active Raman modes, space group, and c/a lattice parameter ratio for the zirconia polymorphs.

Crystal system	Space group	Active raman modes	c/a
Tetragonal	D_{4h}	$A_{1g} + 2B_{1g} + 3E_g$	>1
Cubic	O_h	T_{2g}	=1

$$F(R) = \frac{k}{s} = \frac{(1-R)^2}{2R} \quad (4)$$

where R is the percentage of reflected light. The incident photon energy ($h\nu$) and the optical band gap energy (E_g) are related to the transformed Kubelka–Munk function, $[F(R)\ h\nu]^p = A\ (h\nu - Eg)$, where E_g is the band gap energy, A is a constant depending on the transition probability and p is the power index that is related to the optical absorption process. p equals to 1/2 or 2 for an indirect or a direct allowed transition, respectively.

The E_g values are shown in Fig. 3. Intermediate levels of energy in the band gap region result from the structural defects in ZrO_2 [53]. For example, oxygen vacancies, the type of structural defect that occurs in the present case, are generated in order to compensate for the Zr^{4+} ions replaced by RE^{3+} ions. E_g values of 5.21, 5.09, 5.06, 4.97, and 4.92 eV are obtained for the undoped, 1, 2, 4, and 8 mol.% RE-doped materials, respectively.

In addition, the calculated values of the cell parameters concur with the experimentally determined results (a = 5.127 Å for the cubic phase, and a = 3.630 Å and c = 5.264 Å for the tetragonal phase). The results of the theoretical calculations indicate that, in both the cubic and tetragonal structures, 12% of Eu produces a local distortion that is both centered on the dopant, and located near the oxygen vacancy (Vo). The geometry of doped ZrO_2 with Eu^{+3}

showing the coordination polyhedra of the cubic and tetragonal phases is shown in Fig. 4.

The vacancy corresponding to an O atom missing from the structure was examined by taking into account the proximity of the Eu atoms. For both phases, large distances between the oxygen vacancy and the Eu atoms, constitute more favorable arrangements than other configurations. Consequently, some Zr atoms are seven-coordinated in the case of the cubic phase and are also neighbored by an Eu atom in the case of the tetragonal phase (see Table 3).

The difference between the formation energies of the cubic and tetragonal phases ($\Delta E_{C\text{-}T}$) of ZrO_2 and $Zr_{0.88}Eu_{0.12}O_{1.94}$ are 0.84 eV and −0.34 eV, respectively. These results indicate that the incorporation of Eu into the ZrO_2 structure increases the already higher stability of the cubic phase, relative to that of the tetragonal phase. This explains the preferential Eu doping of the cubic phase of the films.

We used a supercell model in which the cubic and tetragonal phases are each assigned 48 atoms, to determine the effect of Eu incorporation into the ZrO_2 lattice, on the electronic structure. The total and projected density of states (DOS) of the atoms and orbitals of the pure and doped cubic phase are shown in Fig. 5; the results corresponding to the pure and doped tetragonal phase are shown in Fig. 6.

The top of the VB and the bottom of the conduction band (CB) are composed mainly of O 2p levels and Zr 4d levels, respectively. Furthermore, E_g values of 3.21 eV and 3.83 eV were calculated for the respective undoped cubic and undoped tetragonal phases. These values are both lower than their experimentally determined counterparts. However, compared to the former (3.21 eV), the latter (3.83 eV) is closer to E_g of the pure ZrO_2 (5.21 eV), investigated in this work. A comparison of the electronic structures shown in Figs. 5(b) and 6(b) reveals that Eu doping leads to a systematic decrease in E_g and an increase in the density of electronic states inside the gap. Moreover, the effect of Tb and Tm incorporation into the ZrO_2 lattice has been also explored, and the total and projected density of states on atoms for doped Tb and Tm, in cubic and tetragonal phases, are shown in Fig. S1 of Supplementary Information. Therefore, the theoretical calculations indicate that these states occur in the forbidden zone of energy, owing to the presence of Eu, Tb and Tm transition metals and O vacancies in the ZrO_2 lattice.

3.4. PL studies

The optical properties of Eu dopants in various host materials, have been characterized [54–62]. Owing to the hypersensitivity of the $^5D_0 \rightarrow {}^7F_2$ transition, Eu ions can be used to monitor morphological changes in the host material, which are induced by external stimuli [63–66].

Fig. 7 shows the PL spectra of both the undoped and co-doped ZrO_2. The band in the emission spectrum of undoped ZrO_2 ranges from 376 nm to 648 nm with a peak centered at 460 nm, as shown in Fig. 7. This is attributed to the $(O^{2-})\ p \rightarrow d\ (Zr^{4+})$-type transition [53], which results from a sequence of non-radiative relaxations of localized electrons in the CB; this is followed by band recombination within the band gap, and subsequent decrease in energy of the electrons when they move to the VB [67]. Factors such as the particle size and morphology, crystallinity, and the method of synthesis [68,69] may influence the photoluminescent properties of the zirconia.

The PL spectra of ZrO_2:RE (RE = Tm^{3+}, Tb^{3+}, and Eu^{3+}) powders exhibit characteristics of each dopant-ion emission. For example, in the case of excitation at 350 nm, the emission peak at 477 nm is attributed to Tm^{3+}, which is associated with the $^1G_4 \rightarrow {}^3H_6$ transition [70,71]. The $^5D_4 \rightarrow {}^7F_6$ and $^5D_4 \rightarrow {}^7F_5$ transitions occur at wavelengths of 496.02 nm and 548.32 nm, respectively, and are associated with the emission of Tb^{3+} [72,73]. In addition, the Eu^{3+}, $^5D_0 \rightarrow {}^7F_1$, and $^5D_0 \rightarrow {}^7F_2$ transitions occur at respective wavelengths of 597.16 nm and 617.54 nm [74,75]. The interference of the host has a more significant effect on the photoluminescent behavior of ZrO_2:8%RE than on the behavior of ZrO_2. This effect is manifested as the occurrence of a broad band at wavelengths ranging from 380 nm to 480 nm, and results from the structural defects in ZrO_2. The order-disorder effects in the coordination of some Zr and doped atoms, verified by theoretical calculations, can result in the production of new levels between the valence and the conduction bands, which favor the PL emission properties. As Fig. 7(c) shows, the emission intensity of the Eu^{3+} ions increases with increasing

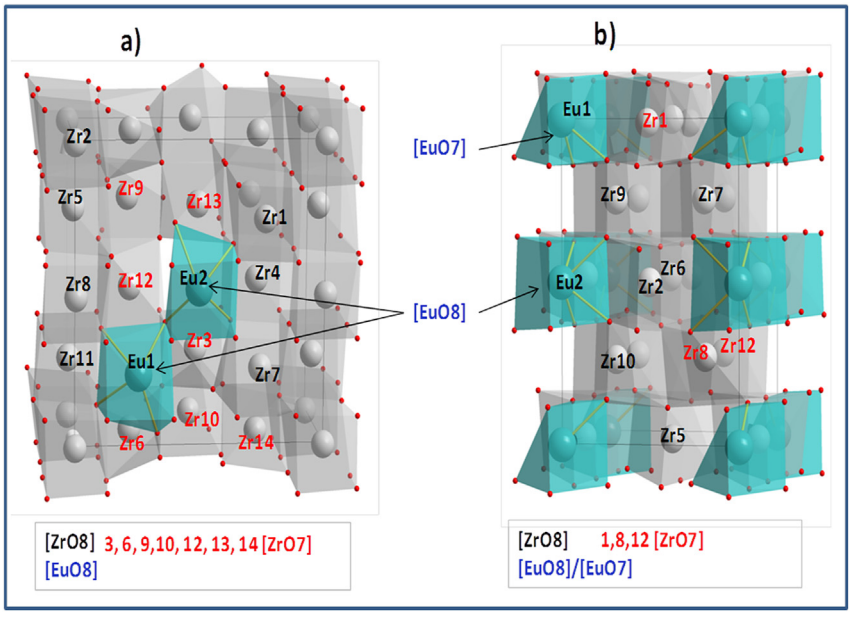

Fig. 4. Geometry of doped ZrO2 with Eu^{3+} showing the coordination polyhedral: a) cubic phase and b) tetragonal phase.

Table 3
Distances in A for the coordination polyhedra for doped ZrO_2 with Eu^{3+} for the cubic and tetragonal phases.

Cubic					Tetragonal				
Symbol	Ligands	Faces	Dmin	Dmax	Symbol	Ligands	Faces	Dmin	Dmax
Eu1	8	12	2.281	2.471	Eu1	7	8	2.286	2.368
Eu2	8	10	2.308	2.459	Eu2	8	11	2.331	2.512
Zr1	8	12	2.071	2.611	Zr1	7	10	2.044	2.394
Zr2	8	12	2.061	2.568	Zr2	8	12	2.081	2.48
Zr3	7	9	2.079	2.184	Zr3	8	12	2.063	2.617
Zr4	8	10	2.091	2.265	Zr4	8	12	2.055	2.501
Zr5	8	12	2.066	2.487	Zr5	8	12	2.108	2.376
Zr6	7	10	2.054	2.218	Zr6	8	12	2.141	2.269
Zr7	8	12	2.141	2.347	Zr7	8	12	2.118	2.391
Zr8	8	12	2.11	2.326	Zr8	7	10	2.071	2.297
Zr9	7	9	2.006	2.303	Zr9	8	12	2.127	2.44
Zr10	7	10	2.041	2.267	Zr10	8	12	2.098	2.685
Zr11	8	12	2.131	2.268	Zr11	8	12	2.118	2.391
Zr12	7	10	2.089	2.206	Zr12	7	10	2.071	2.297
Zr13	7	9	2.058	2.219	Zr13	8	12	2.127	2.44
Zr14	7	10	2.069	2.261	Zr14	8	12	2.098	2.685

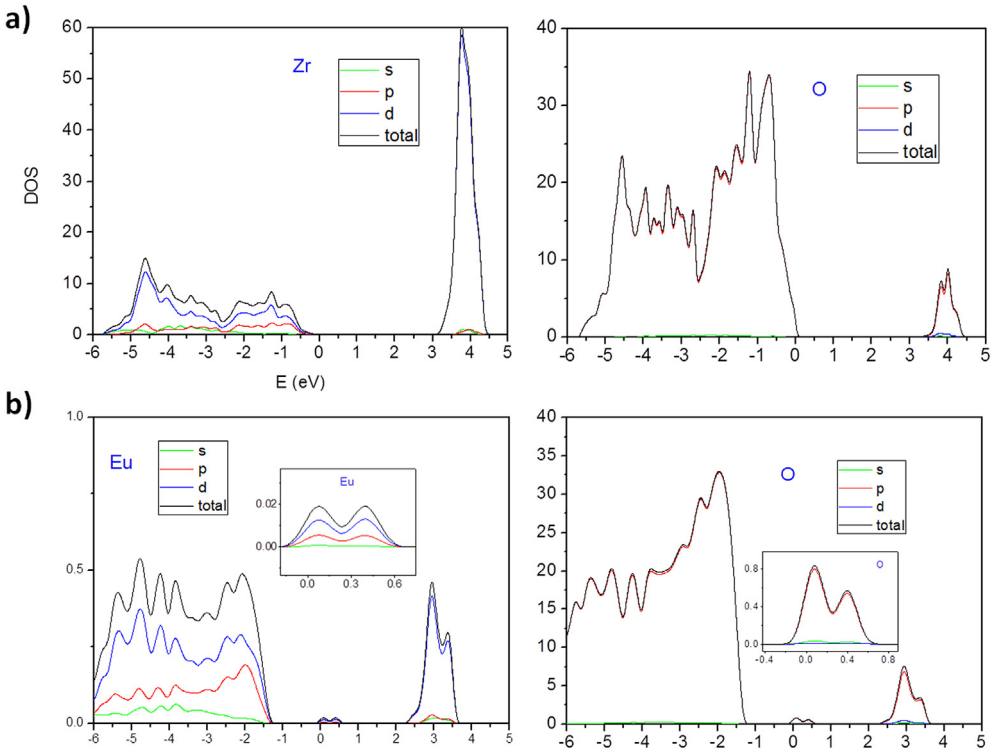

Fig. 5. Total and projected density of states on atoms and orbitals for the pure (a) and doped cubic phase (b).

concentration of Eu^{3+}, reaches a maximum at 4 mol.% RE, and decreases thereafter (owing to the quenching effect) [76]. The critical quenching concentration of Eu^{3+} is defined as the concentration at which the emission intensity begins to decrease. Similarly, the critical distance, corresponding to the critical quenching concentration, is defined as the average distance between the nearest Eu^{3+} ions, at which energy transfer processes occur.

3.5. Energy transfer in ZrO_2:RE (RE = Tm^{3+}, Tb^{3+}, and Eu^{3+}) powders

A schematic energy level diagram illustrating Tm^{3+}, Tb^{3+}, and Eu^{3+} absorption, non-radiative relaxation, and processes leading to blue, green, and red emissions is shown in Fig. 8. The energy level $^5D_4$ of Tb^{3+} is very close to the energy level of Tm^{3+} $^1G_4$ as seen in the energy diagram (Fig. 8). This setting energy levels contributes to efficient energy transfer process (ET1) between Tm^{3+} ions and Tb^{3+} [77]. The $^1G_4$ level of Tm^{3+} is completely filled by the charge carriers (electrons) from the excitation process (λ = 350 nm). The increased concentration of Tm^{3+} promotes the increase of the intensity of the transition $^1G_4 \rightarrow {}^3H_6$, this increased intensity of Tm^{3+} also acts as a source for transporting energy for the sublevel $^5D_4$ of Tb^{3+}, this effect is realized by increasing the intensity of transition $^5D_4 \rightarrow {}^7F_5$ (550 nm) Tb^{3+}, shown in Fig. 7.

The Energy transfer (ET2) between Tb^{3+} and Eu^{3+} has been extensively studied, in order to understand the photoluminescent behavior [78]. In fact, the luminescence intensities of various rare-earth ions can be enhanced or quenched by the energy transfer

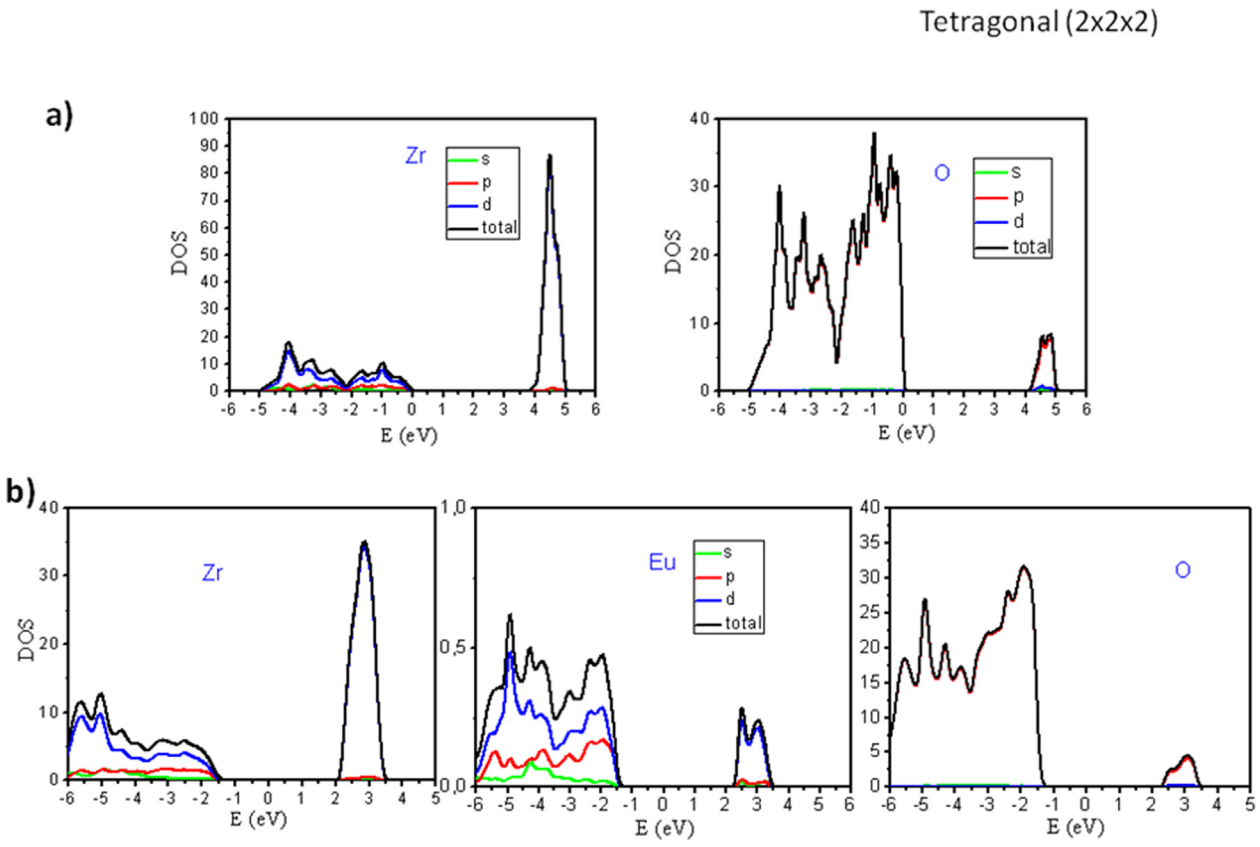

Fig. 6. Total and projected density of states on atoms and orbitals for the pure (a) and doped tetragonal phase (b).

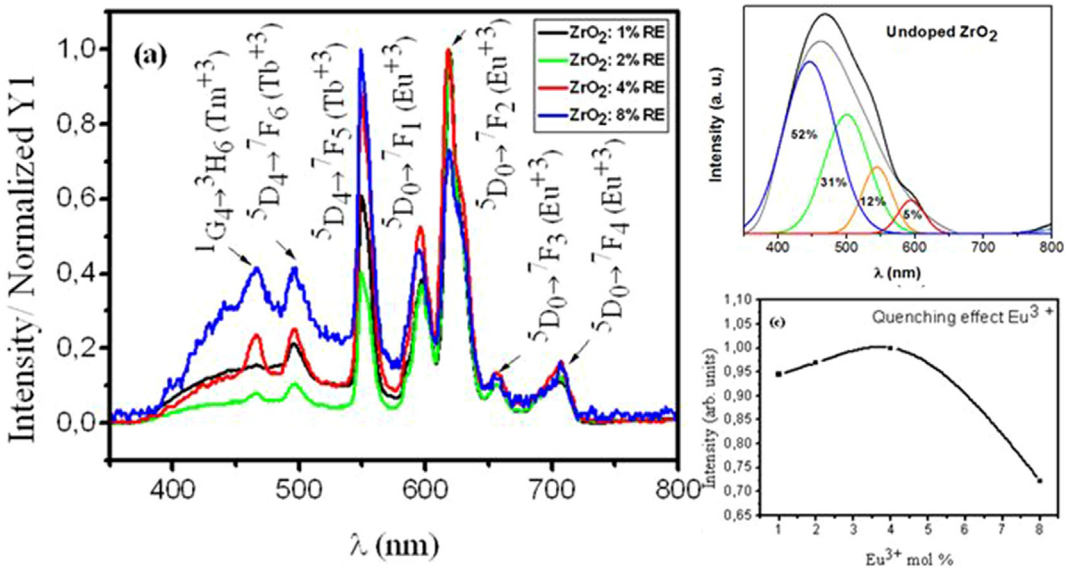

Fig. 7. Photoluminescence emission spectra of (a) ZrO_2:xRE (x = 1–8 mol%), (b) undoped ZrO_2, (c) quenching effect in the transition $^5D_0 \rightarrow {}^7F_1$ (Eu^{3+}) at 617.54 nm.

from other co-doped rare-earth ions [79–81]. ET2 between Tb^{3+} and Eu^{3+} may occur in hosts, such as tungstates, zeolite-Y, yttria, porous silicon, borate, hydrate, and molybdates [82–85]. The probability of this transfer is proportional to R^{-6} (R: average distance between Tb^{3+} and Eu^{3+}), and hence the efficiency of the ET2 process increases gradually with increasing Eu^{3+}-doping concentration. Furthermore, R decreases with increasing Eu^{3+} concentration and therefore, the energy transfer efficiency of $Tb^{3+} \rightarrow Eu^{3+}$ increases. Owing to the quenching effect, this behavior is not unique to the ZrO_2:8% RE, as shown in Fig. 7(c).

An analysis of the results depicted in Fig. 8 renders that electrons on Tb^{3+} ions are promoted from the ground state ($4f^8$) to the excited state ($4f^75d$), by 350.7-nm UV light. These electrons then relax to the lowest excited state $^5D_4$, by means of a multi-phonon

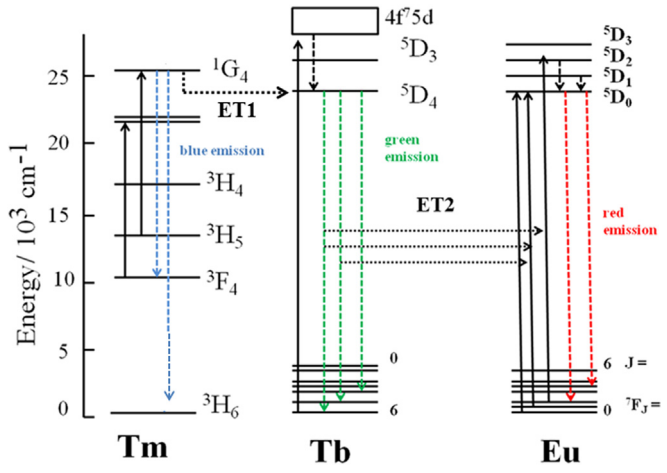

Fig. 8. Schematic diagram of the Tm^{3+}, Tb^{3+}, and Eu^{3+} energy levels and the processes leading to blue, green, and red emission. (For interpretation of the references to colour in this figure legend, the reader is referred to the web version of this article.)

relaxation process. The electrons may return to the ground state, thereby resulting in Tb^{3+} emissions ($^5D_4 \rightarrow {}^7F_{6,5,4}$). Alternatively, their excitation energy may be transferred from the $^5D_4$ (Tb^{3+}) level to the higher excited energy levels of Eu^{3+} ($4f^6$) through cross relaxation; these levels then relax to the $^5D_0$ (Eu^{3+}) level, thereby resulting in red-orange emissions ($^5D_0 \rightarrow {}^7F_{0,1,2}$). The $^5D_4 \rightarrow {}^7F_{6,5,4,3}$ emissions of Tb^{3+} overlap with the $^7F_{0,1} \rightarrow {}^5D_{0,1,2}$ absorptions of Eu^{3+} and hence, the energy transfer from Tb^{3+} to Eu^{3+} is, in general, very efficient.

Fig. 9 shows the CIE coordinates of ZrO_2:xRE (1–8 mol.%), while Table 4 lists the CIE coordinate values and CCT values for samples ZrO_2:xRE (1–8 mol.%). We obtained white light emission from a single component, by co-doping the ZrO_2 host with Tm^{3+}, Tb^{3+}, and Eu^{3+} ions. Under the excitation of UV light, a full-color emission is obtained, resulting from the simultaneous blue, green, and red

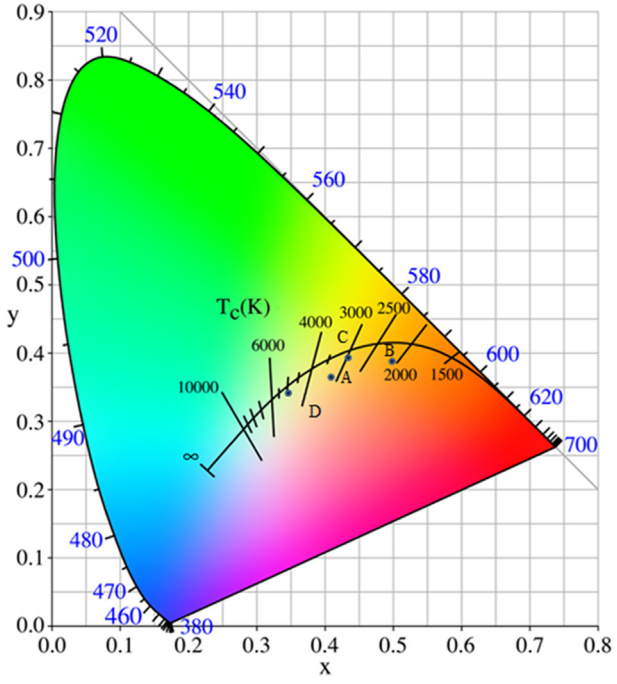

Fig. 9. CIE chromaticity diagram for ZrO_2:xRE (x = 1, 2, 4, and 8 mol%).

Table 4
Chromaticity coordinates and correlated temperature color for ZrO_2:xRE (x: 1, 2, 4 and 8 mol%).

Sample	x	y	CCT (K)	Color
ZrO_2: 1% Eu	0.41	0.36	3.174	Yellow
ZrO_2: 2% Eu	0.50	0.37	1.988	Orange
ZrO_2: 4% Eu	0.43	0.38	2.917	Yellow
ZrO_2: 8% Eu	0.34	0.34	5.181	White

emission of the Tm^{3+}, Tb^{3+}, and Eu^{3+} ions. It is observed in Fig. 7, for the sample ZrO_2: 8% RE, the photoluminescent behavior of ZrO_2 host was very significant. The presence of oxygen vacancies (V_0) in the matrix is responsible for the emergence of broadband emission at around 450 nm [86]. The oxygen vacancy always leads to formation of energy levels within the band gap. When ZrO_2 is excited by a photon, the electrons are trapped by V_0 and centers are created (F) [87]. Then recombination centers (F) with the holes (h^+) creates the transmitter excited states. From these states originate transitions which decay to a state with lower energy level. The band of blue emission from the ZrO_2 contributes along with the specific emission of rare earth on white emission as shown in Fig. 8. A single-composition white-emitting phosphor is therefore obtained. In fact, this white emission occurs independent of the excitation, depends on the doping concentration of the rare-earth ions, and is obtained by blending the aforementioned simultaneous emissions. The emissions are characterized by the colors emitted from each sample. This characteristic is defined by chromaticity coordinates x and y.

4. Conclusions

ZrO_2:RE powders were successfully obtained via complex polymerization. The phase (i.e., tetragonal) comprising the ZrO_2:xRE (x: 1, 2, and 4 mol.%) samples was identified via XRD analysis, whereas the cubic phase, stabilized in ZrO_2:8%RE, was identified via Raman spectroscopy. The structural and electronic effects, resulting from Eu in both the cubic and tetragonal ZrO_2:Eu^{3+} phases, were explained by calculating (using DFT) the relevant energies. The photoluminescence emission spectra reveal transitions of the type: $^1G_4 \rightarrow {}^3H_6$ (477 nm), $^5D_4 \rightarrow {}^7F_{5,6}$ (496.02 nm and 548.32 nm), and $^5D_0 \rightarrow {}^7F_{1,2}$ (597.16 nm and 617.54 nm) from Tm^{3+}, Tb^{3+}, and Eu^{3+}, respectively. An inter-level energy transfer, $^5D_4$ (Tb^{3+}) $\rightarrow$ $^5D_1$ (Eu^{3+}), also occurred. In addition, according to the CIE diagram, the CIE coordinates (x: 0.34 and y: 0.34) calculated for ZrO_2: 8%RE, correspond to a point that lies in the white region. The results of this work suggest that these materials have significant potential for use in the field of light-emitting diodes.

Acknowledgment

The authors gratefully acknowledge the financial support of the Brazilian governmental research funding agencies CAPES, CNPq 402127/2013-7, FAPESP 2013/07296-2 and INCTMN 2008/57872-1.

Appendix A. Supplementary data

Supplementary data related to this article can be found at http://dx.doi.org/10.1016/j.jallcom.2016.11.341.

References

[1] F. Auzel, Upconversion and anti-Stokes processes with f and d ions in solids, Chem. Rev. 104 (2004) 139–174.

[2] J.-C.G. Bunzli, Benefiting from the unique properties of lanthanide ions, Acc. Chem. Res. 39 (2006) 53–61.
[3] R. Bazzi, et al., Synthesis and luminescent properties of sub-5-nm lanthanide oxides nanoparticles, J. Luminescence 102–103 (2003) 445–450.
[4] S.M. Hussain, A.M. Schrand, R.C. Murdock, D.M. Mattie, J.J. Schlager, M. Terrones, Toxicity evaluation for safe use of nanomaterials: recent achievements and technical challenges, Adv. Mater. 21 (2009) 1549–1559.
[5] F.T. Wang, Y. Zhang, X. Fan, M. Wang, Luminescent nanomaterials for biological labelling, Nanotechnology 17 (2006) R1–R17.
[6] F.L. Wang, et al., Recent advances in the chemistry of lanthanide doped upconversion nanocrystals, Chem. Soc. Rev. 38 (2009) 976–989.
[7] F. Wang, D. Banerjee, L. Yonqshenq, X. Chen, X. Liu, Upconversion nanoparticles in biological labeling, imaging, and therapy, Analyst 135 (2010) 1839–1854.
[8] J.S. Shen, C. Yan, Luminescent rare earth nanomaterials for bioprobe applications, Dalton Trans. 48 (2008) 5687–5697.
[9] J.L. Zhou, F. Li, Upconversion nanophosphors for smallanimal imaging, Chem. Soc. Rev. 41 (2012) 1323–1349.
[10] D.E.A. Achatz, O.S. Wolfbeis, Luminescent chemical sensing, biosensing, and screening using upconverting nanoparticles, Top. Curr. Chem. 300 (2011) 29–50.
[11] M. Haase, H. Schafer, Upconverting nanoparticles, Angew. Chem. Int. Ed. 50 (2011) 5808–5829.
[12] Y. Yang, Upconversion nanophosphors for use in bioimaging, therapy, drug delivery and bioassays, Microchim. Acta 181 (2014) 263–294.
[13] H.K. Kobayashi, M. Ogawa, N.Y. Morgan, P.D. Smith, C.B. Murray, X. Ye, J. Collins, G.A. Kumar, H. Bell, P.L. Choyke, In vivo multiple color lymphatic imaging using upconverting nanocrystals, J. Mater. Chem. 19 (2009) 6481–6484.
[14] S.H. Wu, D.J. Milliron, S. Aloni, V. Altoe, D.V. Talapin, B.E. Cohen, P.J. Schuck, Non-blinking and photostable upconverted luminescence from single lanthanide-doped nanocrystals, Natl. Acad. Sci. U. S. A. 106 (2009) 10917–10921.
[15] S. Mukherjee, D.P. Dutta, N. Manoj, A.K. Tyagi, Sonochemically synthesized rare earth double-doped zirconia nanoparticles: probable candidate for white light emission, J. Nanopart. Res. 14 (2012) 814.
[16] W. Du, Z. Zhu, X. Zhang, D. Wang, D. Liu, X. Qian, J. Du, RE/ZrO_2 (RE = Sm, Eu) composite oxide nano-materials: synthesis and applications in photocatalysis, Mater. Res. Bull. 48 (2013) 3735–3742.
[17] R. Marin, G. Sponchia, E. Zucchetta, P. Riello, G. De Portu, F. Enrichi, A. Benedetti, Monitoring the t → m martensitic phase transformation by photoluminescence emission in Eu^{3+}-Doped zirconia powders, J. Am. Ceram. Soc. 96 (2013) 2628–2635.
[18] A. Speghini, P. Riello, S. Bucella, A. Benedetti, Preparation, structural characterization, and luminescence properties of Eu^{3+}-doped nanocrystalline ZrO_2, J. Mater. Res. 20 (2005) 2780–2791.
[19] E. De la Rosa, P. Salas, R.A. Rodríguez, Visible light emission under UV and IR excitation of rare earth doped ZrO_2 nanophosphor, Opt. Mater. 27 (2005) 1320–1325.
[20] G. García-Rosales, et al., Energy transfer from Tb^{3+} to Eu^{3+} ions sorbed on $SrTiO_3$ surface, J. Luminescence 132 (2012) 1299–1306.
[21] S. Gai, C. Li, P. Yang, J. Lin, Recent progress in rare earth micro/nanocrystals: soft chemical synthesis, luminescent properties, and biomedical applications, Chem. Rev. 114 (2014) 2343–2389.
[22] Z.W. Quan, J. Lin, Synthesis and characterization of spherical ZrO_2: Eu^{3+} phosphors by spray pyrolysis process, Mater. Res. Bull. 40 (2005) 810–820.
[23] A. Gedanken, E. Sominski, O. Palchik, Y. Koltypin, G. Panczer, M. Gaft, H. Minti, Sonochemical preparation and characterization of europium oxide doped in and coated on ZrO_2 and yttrium-stabilized zirconium (YSZ), J. Phys. Chem. B 104 (2000) 7057–7065.
[24] N. Tiwari, S.R. Kuraria, Effect of variable trivalent europium concentration on photo- and thermoluminescence of zirconium dioxide nanophosphors, Mater. Sci. Semicond. Process. 31 (2015) 214–222.
[25] M. García-Hipólito, O. Álvarez-Fregoso, C. Falcony, M.A. Aguilar-Frutis, Preparation and characterization of Eu doped zirconia luminescent films synthesized by pyrosol technique, J. Mater. Sci. Lett. 20 (2001) 1799–1801.
[26] E. Pereyra-Perea, M. García, Preliminary studies on luminescent terbium doped ZrO_2 thin films prepared by sol-gel process, Phys. D. Appl. Phys. 31 (1998) L7–L10.
[27] H. Zhang, S. Niu, Q. Xin, Blue emission of ZrO_2:Tm nanocrystals with different crystal structure under UV excitation, J. Non-Cryst. Solids 354 (2008) 1559–1563.
[28] Y.S. Vidya, et al., Phase transformation of ZrO_2:Tb^{3+} nanophosphor: color tunable photoluminescence and photocatalytic activities, J. Alloys Compd. 622 (2015) 86–96.
[29] B. Marí, et al., Preparation and luminescence properties of Tb^{3+} doped ZrO_2 and $BaZrO_3$ phosphors, J. Luminescence 130 (2010) 2128–2132.
[30] M. Shang, X. Kang, D. Yang, Y. Zhang, J. Lin, Hydrothermal derived LaOF: Ln^{3+} (Ln = Eu, Tb, Sm, Dy, Tm, and/or Ho) nanocrystals with multicolor-tunable emission properties, Inorg. Chem. 51 (2012) 11106–11116.
[31] B.C. Joshi, Enhanced Eu^{3+} emission by non-radiative energy transfer from Tb^{3+} in zinc phosphate glass, J. Non-Cryst. Solids 180 (1995) 217–220.
[32] S.-H. Yang, et al., Luminescence of CNT coated $LaPO_4$:Tm phosphors and their field emission lamp application, J. Alloys Compd. 612 (2014) 210–214.
[33] A.A. Ansari, et al., Structural and photoluminescence properties of Tb-doped $CaMoO_4$ nanoparticles with sequential surface coatings, Mater. Chem. Phys. 147 (2014) 715–721.
[34] X. Zhou, et al., $LiY_{1-x}Eu_x(MoO_4)_2$ as a promising red-emitting phosphor of WLEDs synthesized by sol-gel process, J. Rare Earths 30 (2012) 315–319.
[35] J.C. Zhang, et al., White light emitting glasses, J. Solid State Chem. 93 (1991) 17–29.
[36] C. Zhu, et al., Luminescence properties of Tb doped and Tm/Tb/Sm co-doped glasses for LED applications, J. Luminescence 130 (2010) 74–77.
[37] P.N. Medeiros, A.P. Marques, R.L. Tranquilin, C.A. Paskocimas, M.R.D. Bomio, J. A.Varela, E. Longo, F.V. Motta, Effect of different starting materials on the synthesis of $Ba_{0.8}Ca_{0.2}TiO_3$, J. Adv. Ceram. 65 (2015) 65.
[38] V.D. Araujo, F.V. Motta, A.P. Marques, Effect of calcium on the structural properties of $Ba_{(1-x)}Ca_xTiO_3$ particles synthesized by complex polymerization method, J. Mater Sci. 49 (2014) 2875.
[39] F.V. Motta, A.P. Marques, J.W.M. Espinosa, P.S. Pizani, E. Longo, J.A. Varela, Room temperature photoluminescence of BCT prepared by complex polymerization method, Curr. Appl. Phys. 10 (2010) 16.
[40] T.M. Mazzo el at, Photoluminescence properties of $CaTiO_3$:Eu^{3+} nanophosphor obtained by the polymeric precursor method, Mater. Chem. Phys. 145 (2014) 141.
[41] E.F. Schubert, Light Emitting Diodes, Cambridge University Press, 2003.
[42] R. Robertson, Computation of correlated color temperature and distribution temperature, J. Opt. Soc. Am. 58 (1968) 1528.
[43] C. S. McCamy. Correlated Color Temperature as an Explicit Function of Chromaticity Coordinates, Wappingers Falls, New York 12590-1804.
[44] J.P. Perdew, K. Burke, Rationale for mixing exact exchange with density functional approximations, J. Chem. Phys. 105 (1996) 9982–9985.
[45] S. Das, et al., Structural and optical properties of tunable warm-white light-emitting ZrO_2:Dy^{3+}–Eu^{3+} nanocrystals, J. Am. Ceram. Soc. 96 (2013) 1602–1609.
[46] N. Shibata, A. Kuwabara, Y. Ikuhara, T. Sakuma, The instability and resulting phase transition of cubic zirconia, Mater. Sci. Eng. A 302 (2001) 90–98.
[47] H.P. Klug, X-ray Diffraction Procedures for Polycrystalline and Amorphous Materials, John Wiley & Sons, New York, 1962, pp. 491–538.
[48] E.W. Nuffield, Diffraction Procedures Methods, John Wiley and Sons, New York, 1986, pp. 147–148.
[49] C.G. Kontoyannis, Quantitative determination of the cubic, tetragonal and monoclinic phases in partially stabilized zirconias by Raman spectroscopy, J. Mater. Sci. 29 (1994) 5316–5320.
[50] D. Bersani, et al., Micro-Raman study of indium doped zirconia obtained by sol–gel, J. Non-Cryst. Solids 345–346 (2004) 116–119.
[51] C. Wulfman, M. Sadoun, M. Lamy de la Chapelle, Interest of Raman spectroscopy for the study of dental material: the zirconia material example, IRBM 31 (2010) 257–262.
[52] P. Kubelka, F. Munk-Aussig, Ein beitrag zur optick der farbanstriche, Z. Tech. Phys. 12 (1931) 593–601.
[53] M.D. Gonçalves, et al., (Sr,Tm)ZrO_3 powders prepared by the polymeric precursor method: synthesis, optical properties and morphological characteristics, Opt. Mater. 31 (2009) 1134–1143.
[54] B. Bihari, H. Eilers, B.M. Tissue, Spectra and dynamics of monoclinic Eu_2O_3 and Eu^{3+}:Y_2O_3 nanocrystals, J. Luminescence 75 (1997) 1–10.
[55] R. Debnath, A. Nayak, A. Ghosh, On the enhancement of luminescence efficiency of Y_2O_3:Eu^{3+} red phosphor by incorporating (Al^{3+}, B^{3+}) in the host lattice, Chem. Phys. Lett. 444 (2007) 324–327.
[56] H. Eilers, B.M. Tissue, Laser spectroscopy of nanocrystalline Eu_2O_3 and Eu^{3+}:Y_2O_3, Chem. Phys. Lett. 251 (1996) 74–78.
[57] X.R.Z. Hou, Y.K. Li, W.J. Li, Luminescent properties of nano-sized Y_2O_3:Eu fabricated by co-precipitation method, J. Alloy Compd. 494 (2010) 382.
[58] J. Guohua, Local site symmetry determination of scheelite-type structures by Eu^{3+} spectroscopy, J. Phys. Chem. C 114 (2010) 17905–17913.
[59] M. Jia, et al., UV excitation properties of Eu^{3+} at the S6 site in bulk and nanocrystalline cubic Y_2O_3, Chem. Phys. Lett. 384 (2004) 193–196.
[60] X. Qu, B.K. Moon, B.C. Choi, J.H. Jeong, K.H. Kim, Preparation and photoluminescence properties of Gd_2O_3:Eu^{3+} inverse opal photonic crystals, J. Phys. Chem. C 114 (2010) 19891.
[61] C. Shang, X. Shang, M. Li, L. Zhao, Investigation on the luminescence improvement of nanosized La_2O_3/Eu^{3+} phosphor under charge-transfer excitation, J. Phys. Chem. C 115 (2011) 2630–2635.
[62] C. Shang, et al., Investigation on the red shift of charge transfer excitation spectra for nano-sized Y_2O_3:Eu^{3+}, Chem. Phys. Lett. 501 (2011) 480–484.
[63] K. Binnemans, Lanthanide-based luminescent hybrid materials, Chem. Rev. 109 (2009) 4283–4374.
[64] K. Binnemans, C. Görller-Walrand, A simple model for crystal field splittings of the $^7F_1$ and $^5D_1$ energy levels of Eu^{3+}, Chem. Phys. Lett. 245 (1995) 75–78.
[65] G. Blasse, The Eu^{3+} luminescence as a measure for chemical bond differences in solids, Chem. Phys. Lett. 20 (1973) 573.
[66] T. Myint, H. Eilers, Light-induced structural changes in Eu-doped (Pb,La)(Zr,Ti)O_3 ceramics, Appl. Phys. Lett. 98 (2011) 171906.
[67] J. Liang, X. Jiang, Y. Li, Photoluminescence of tetragonal ZrO_2 nanoparticles synthesized by microwave irradiation, Inorg. Chem. 41 (2002) 3602.
[68] L.J. Lai, H.K. Chen, M.B. Cheng, M.I. Lin, T.C. Chun, Photoluminescence of zirconia films with VUV excitation, J. Electron Spectrosc. Relat. Phenom. 865 (2005) 144–147.
[69] L. Kumari, J.M. Xu, R.M. Leblanc, D.Z. Wang, Y. Li, H. Guo, J. Zhang, Controlled hydrothermal synthesis of zirconium oxide nanostructures and their optical

properties, Cryst. Growth Des. 9 (2009) 3874–3880.
[70] J.W. Shur, K.H. Choi, D.H. Yoon, Growth of Zr co-doped Tm:$LiNbO_3$ single crystal for improvement of photoluminescence property in blue wavelength range, J. Cryst. Growth 318 (2011) 653–656.
[71] H. Zhang, et al., Photoluminescence of YVO_4:Tm phosphor prepared by a polymerizable complex method, Solid State Commun. 132 (2004) 527–531.
[72] Y. Xie, L. Liu, Y. Su, H. Zhao, Y. Liu, Z. Zhang, H. Duan, J. Li, E. Xie, Oxygen defects-modulated green photoluminescence of Tb-doped ZrO_2 nanofibers, Appl. Phys. Lett. 97 (2010) 141916.
[73] R.E. Muenchausen, et al., Effects of Tb doping on the photoluminescence of Y_2O_3:Tb nanophosphors, J. Luminescence 126 (2007) 838–842.
[74] R.K. Tamrakar, D.P. Bisen, K. Upadhyay, Photoluminescence behavior of ZrO2: Eu^{3+} with variable concentration of Eu^{3+} doped phosphor, J. Radiat. Res. Appl. Sci. 8 (2015), 11–1675.
[75] M. Najafi, H. Haratizadeh, The effect of growth conditions and morphology on photoluminescence properties of Eu-doped ZnO nanostructures, Solid State Sci. 41 (2015) 48–51.
[76] O. Meza, L.A. Diaz-Torres, H. Desirena, J.L. Rodríguez-Lopez, Luminescence concentration quenching mechanism in Gd2O3:Eu3+, J. Phys. Chem. A 118 (2014) 1390–1396.
[77] C.P. Wyss, M. Kehrli, Th. Huber, P.J. Morris, W. LuKthy, H.P. Weber, A.I. Zagumennyi, Y.D. Zavartsev, P.A. Studenikin, I.A. Shcherbakov, A.F. Zerrouk, Excitation of the thulium $^1G_4$ level in various crystal hosts, J. Luminescence 82 (1999) 137–144.
[78] T.K. Anh, N. Vu, et al., Nanomaterials containing rare-earth ions Tb, Eu, Er and Yb: preparation, optical properties and application potential, J. Luminescence 102–103 (2003) 391–394.
[79] G. Li, Z. Hou, C. Peng, Z. Cheng, J. Lin, Nanocrystalline LaOCl:Tb^{3+}/Sm^{3+} as promising phosphors for full-color field-emission displays, Opt. Lett. 34 (2009) 3833–3835.
[80] A.G. Macedo, D. Ananias, M.V. Reis, V.S. Amaral, L.D. Carlos, J. Rocha, Effects of phonon confinement on anomalous thermalization, energy transfer, and upconversion in Ln^{3+}-doped Gd_2O_3 nanotubes, Adv. Funct. Mater. 20 (2010) 624–634.
[81] B.H. Lee, et al., The effect to Tb^{3+} Co-doping on the photoluminescence of $(Sr,Ba)_2SiO_4$:Eu^{2+}, J. Electrochem. Soc. 157 (2010) 227–232.
[82] W.W. Holloway, M. Kestigian, R. Newman, Direct evidence for energy transfer between rare earth ions in terbium-europium tungstates, Phys. Rev. Lett. 11 (1963) 458–460.
[83] W. Chen, Y. Huang, Photoluminescence and photostimulated luminescence of Tb^{3+} and Eu^{3+} in zeolite-Y, J. Appl. Phys. 88 (2000) 1424–1431.
[84] K. Anh, et al., Energy transfer between Tb^{3+} and Eu^{3+} in Y_2O_3 crystals, J. Luminescence 39 (1988) 215–221.
[85] J. Yang, C. Li, Y. Yu, Y. Lin, Energy transfer and tunable luminescence properties of Eu^{3+} in $TbBO_3$ microspheres via a facile hydrothermal process, Inorg. Chem. 47 (2008) 7262–7270.
[86] C. Lin, C. Zhang, Jun Lin, Phase transformation and photoluminescence properties of nanocrystalline ZrO_2 powders prepared via the pechini-type sol-gel process, J. Phys. Chem. C 111 (2007) 3300–3307.
[87] A.A. Benyagoub, Mechanism of the monoclinic-to-tetragonal phase transition induced in zirconia and hafnia by swift heavy ions, Phys. Rev. B 72 (2005) 094114.